# Impact of Cloud Vertical Structure Perturbations on the Retrieval of Cloud Optical Thickness and Effective Radius from FY4A/AGRI

Jing Sun<sup>1,2</sup>, Yunying Li<sup>1,3</sup>, Hao Hu<sup>4</sup>, Qian Li<sup>1,3</sup>, Chengzhi Ye<sup>5</sup>, Yi-ning Shi<sup>4</sup>, Zitong Chen<sup>1</sup>

- 1 College of Meteorology and Oceanography, National University of Defense Technology, Changsha 410073, China
- 2 China Meteorological Administration Basin Heavy Rainfall Key Laboratory/Hubei Key Laboratory for Heavy Rain Monitoring and Warning Research, Institute of Heavy Rain, China Meteorological Administration, Wuhan 430205, China
- 3 Key Laboratory of High Impact Weather(special), China Meteorological Administration, Changsha 410073, China
- 4 State Key Laboratory of Severe Weather Meteorological Science and Technology, CMA Earth System Modeling and Prediction Centre, Beijing 100081, China
- 5 Institute of Meteorological Sciences of Hunan Province, Hunan Meteorological Bureau, Changsha 410118, China

Correspondence: Yunying Li (ghlyy@mail.iap.ac.cn)

5

10

20

25

30

Abstract. The vertical structure of clouds plays a critical role in atmospheric radiative transfer and is a major source of uncertainty in satellite-based retrievals of cloud optical thickness (COT) and cloud effective radius (CER). Most operational algorithms assume a single homogeneous layer, but the biases introduced by this simplification under realistic multilayer conditions remain poorly quantified. This study systematically investigates how perturbations in cloud vertical structure affect COT and CER retrievals using FY4A/AGRI (Advanced Geostationary Radiation Imager) and simulations from Advanced Radiative Transfer Modeling System (ARMS) over central and eastern China during June–August 2018. We designed ten sensitivity experiments by varying water and ice content across single-, double-, and triple-layer cloud configurations to quantify the impact of structural differences on channel reflectance and the COT-CER relationship. The results indicate that upper-level ice clouds significantly mask reflectance from lower water clouds, reducing total reflectance by approximately 50% and leading to systematic retrieval biases: single-layer algorithms underestimate COT at small CER (<10 µm) but overestimate it by approximately 20 units under larger CER conditions. In single-layer clouds, variations in low- and mid-level water content produce mean COT increases ~24% larger than in double-layer structure, with similar biases occurring in three-layer clouds. Furthermore, enhanced mid-level liquid

water enhances the nonlinear relationship between COT and CER, increasing retrieval uncertainties. These findings identify cloud vertical heterogeneity as a major source of retrieval bias and emphasize the necessity of integrating multilayer cloud information into satellite retrieval algorithms.

#### 1 Introduction

35

40

45

50

55

60

Clouds cover approximately 67% of the Earth's surface on average (Fang et al., 2016) and exert a pivotal influence on the evolution of weather systems and the global hydrological cycle (Matus et al., 2017). The pronounced spatial heterogeneity of clouds introduces substantial uncertainties in their microphysical properties, which is turn complicates the interactions between clouds and radiation. This uncertainty remains a critical limitation in the accuracy of climate change projections and the performance of numerical weather prediction models (IPCC, 2021). The radiative characteristics of clouds are highly sensitive to the physical attributes of cloud particles, particularly variations in key parameters including cloud effective radius (CER), cloud optical thickness (COT), cloud water content, cloud top height, and cloud base height (Wang et al., 2018; Letu et al., 2020). Among these, COT and CER are two important cloud microphysical parameters that govern the cloud's ability to scatter and absorb solar radiation.

With the advancement of satellite technology, satellite observations have become a powerful tool for capturing the spatial and temporal variations of COT and CER on both regional and global scales (Zhao et al., 2018). Mainstream operational retrieval methods are based on the classic bispectral reflectance technique (Nakajima and King, 1990), which serves as the foundation for many operational cloud optical and microphysical products derived from spectral imagers such as MODIS, AHI, and AGRI (Platnick et al., 2003; Min et al., 2017; Letu et al., 2020; Chen et al., 2020; Zhuge et al., 2021; Liu et al., 2023). Although these methods are well established, they typically assume a single homogeneous cloud layer within each satellite pixel. However, the errors introduced by this simplification under realistic atmospheric conditions remain poorly quantified. The accuracy of these retrievals largely depends on the precision of radiative transfer modeling and the adequacy of cloud optical property characterization. Radiative transfer models simulate the top-of-atmosphere radiance observed by satellites by accounting for atmospheric absorption, scattering, and emission processes under various meteorological conditions, and thus serve as the physical foundation for developing satellite-based cloud retrieval algorithms (RTTOV: Saunders et al., 2018; CRTM: Chen et al., 2008; ARMS: Weng et al., 2020).

In reality, clouds are often composed of multiple vertically arranged layers with distinct microphysical properties, including phase type, droplet size variability, and spatial structure. Based on combined

CALIPSO and CloudSat observations, Li et al. (2011) reported that overlapping clouds occur with a global probability of up to 25.8%. Yuan and Oreopoulos (2013) found that approximately 30% of low-level clouds are obscured by upper-level clouds, with overlapping cloud occurrence exceeding 90% in tropical regions. Among these, the typical two-layer cloud system composed of upper-level ice clouds and lower-level water clouds is the most prevalent type, accounting for over 50% of overlapping cloud cases (Sourdeval et al., 2016). Therefore, ignoring the vertical complexity of clouds inevitably introduces retrieval biases in COT and CER retrievals. For instance, Huang et al. (2005) demonstrated using satellite, ground-based microwave radiometer, and lidar observations that the single-layer assumption can lead to a 30% overestimation in COT. In addition, Wang et al. (2019) showed that vertical heterogeneity within ice clouds can result in large underestimations (up to –50%) of MODIS ice water path in deep convective and high-latitude regions, although the effect on global-mean cloud radiative properties is relatively small.

To reduce these biases, Teng et al. (2020) developed a novel multilayer retrieval algorithm that leverages differential absorption across four shortwave infrared channels (0.87, 1.61, 2.13, and 2.25 µm). This method enables simultaneous retrievals of COT and CER for both upper ice and lower liquid layers in ice-over-water cloud systems, significantly improving the agreement between simulated and observed reflectance. More recently, Teng et al. (2023) further advanced this framework by incorporating additional spectral constraints, thereby enhancing the robustness of multilayer cloud retrievals under complex atmospheric conditions. Despite these advances, major challenges remain. In particular, Uncertainties remain in how vertical variations in cloud structure—such as inhomogeneity, overlap, and alignment—affect satellite retrievals of COT and CER. Neglecting these variations can bias simulated radiative effects and heating profiles, underscoring the need for better representation of vertical structure in retrieval algorithms and climate models (Wang et al., 2021).

Although multilayer cloud retrieval algorithms have made significant progress, systematic quantification of how perturbations in cloud vertical structure affect the retrieval of COT and CER remains limited, and assessments of the systematic biases arising from neglecting vertical heterogeneity are still lacking. To address this gap, COT and CER were retrieved using a bispectral lookup table constructed with the ARMS, driven by FY4A/AGRI observations over central and eastern China from June to August 2018. The retrieved results were subsequently validated using MODIS cloud products. On this basis, ten sensitivity experiments were designed to evaluate the retrieval uncertainties directly induced by perturbations in cloud vertical structure, and to reveal the systematic differences between the

COT-CER relationships obtained from multilayer cloud simulations and those derived under the singlelayer assumption. The results enhance the understanding of the mechanisms underlying cloud remote sensing retrievals and offer insights that can guide more accurate interpretation and application of COT and CER retrievals under complex multilayer cloud conditions.

This paper is organized as follows: Section 1 outlines the importance and current progress of satellite-based retrievals of COT and CER. Section 2 describes the data sources and retrieval algorithm. Section 3 presents a validation of the retrieval results against MODIS cloud products. Section 4 investigates the sensitivity of simulated reflectance, COT, and CER to different vertical cloud structures using ARMS. Section 5 summarizes the findings and provides discussion.

## 2 Data, Model and Methods

## 2.1 FY4A/AGRI Data

95

100

105

110

115

120

The satellite data used in this study consist of FY4A/AGRI Level-1 full-disk observations. The FY4A satellite provides high-frequency measurements of the Earth's atmosphere and surface, delivering critical data and products to improve weather forecasting accuracy. Since March 2018, these data have been available for download from the Fengyun Satellite Remote Sensing Data Service Network (https://satellite.nsmc.org.cn/DataPortal/cn/home/index.html). The AGRI instrument onboard FY4A comprises 14 spectral channels, including six visible and near-infrared bands, two mid-infrared bands, two water vapor bands, and four thermal infrared bands. The AGRI completes a full-disk scan every 15 minutes. The spatial resolution ranges from 0.5 to 1.0 km for visible and near-infrared channels, and from 2 to 4 km for infrared channels. The high spatial and temporal resolution of AGRI is advantageous for identifying and tracking small-scale, rapidly evolving systems such as nascent convection (Yang et al., 2017).

To investigate the impact of different vertical cloud structures on COT and CER, satellite observations from June to August 2018 over central China (105°E~120°E, 24°N~39°N) were selected. The retrieval experiments and validations of COT and CER were performed using two spectral channels: visible (0.55–0.75 μm) and shortwave near-infrared (1.58–1.64 μm). Before retrieval, the AGRI data were calibrated using the official coefficients and lookup tables provided in the L1 files, and geometric correction was applied based on the nominal projection, ensuring consistency with operational procedures (https://satellite.nsmc.org.cn/DataPortal/cn/home/index.html).

Previous studies (Sun et al., 2025) indicate that FY-4A/AGRI radiometric calibration exhibits notable seasonal variations, particularly in the shortwave infrared (SWIR) channels (Channels 5 and 6), where the fluctuation indices are 2–4 times larger than those of the visible (VIS) channels due to weaker reflected signals and higher sensitivity to noise. In contrast, VIS channels are relatively stable. During the study period, such uncertainties may propagate through radiative transfer simulations and potentially affect the retrieval of CER. However, cross-validation with MODIS cloud products shows good agreement (see Section 3.1), suggesting that the calibration-related uncertainties of FY-4A/AGRI do not significantly affect the analysis of cloud microphysical characteristics, and the data can be considered reliable for this study.

## 2.2 ARMS Model

125

130

135

140

145

150

This study employs the Advanced Radiative Transfer Modeling System (ARMS) model developed in China, which utilizes a fast transmittance calculation scheme (Weng et al., 2020). In the simulation process, ARMS takes atmospheric optical parameters as inputs, where the optical thickness varies in response to changes in the atmospheric environment. These parameters are typically generated using spectral libraries containing line-by-line absorption coefficients. Optical properties related to five hydrometeor categories—cloud droplets, rain, cloud ice, graupel, snow, and hail are computed for each atmospheric layer. Liquid hydrometeors are assumed to be spherical, and their scattering parameters are derived using Mie theory. Given an effective particle radius, the total number of particles per layer is determined from the hydrometeor water content. For ice clouds, scattering by particles with diameters equal to or larger than the radiation wavelength is treated using the T-matrix method (Bi and Yang, 2017), and the results are stored in a scattering database. The accuracy of the ARMS model has been validated in previous studies (Yang et al., 2020; Tang et al., 2021).

In this study, the ARMS radiative transfer model is employed to simulate cloud reflectance across multiple spectral bands. Atmospheric background fields are sourced from the ERA5 reanalysis dataset (Hersbach et al., 2020), which provides vertical profiles of temperature, water vapor, and ozone, along with pressure levels, cloud liquid and ice water content, surface temperature, and surface type. In addition, a series of idealized sensitivity experiments are conducted by constructing different cloud vertical structures, aiming to investigate the impacts of cloud layering on reflectance, COT, and CER.

## 2.3 COT and CER retrieval

The bispectral retrieval algorithm, developed based on the optical and radiative properties of liquid and ice clouds, is one of the most widely used methods for retrieving cloud parameters. It has been extensively applied to a variety of satellite instruments (Platnick et al., 2017; Min et al., 2017; Letu et al., 2018; Zhuge et al., 2021). In this study, the COT and CER are retrieved using observations from the FY4A/AGRI visible channel (0.65  $\mu$ m) and shortwave near-infrared channel (1.61  $\mu$ m), with forward simulations provided by the ARMS radiative transfer model. The overall retrieval procedure is illustrated in Fig. 1.

Based on the approach proposed by Zhuge et al. (2017), a fast cloud detection algorithm is implemented using AGRI Level-1 data (0.47, 0.65, 0.825, and 1.61 µm) to distinguish between cloudy pixels and clear-sky conditions, with thresholds listed in Table 1. Pixels with brightness temperatures (10.7 µm) below 233 K are classified as ice clouds, and those above 273 K as liquid clouds. ERA5 reanalysis data are interpolated in time and space to match the spatial and temporal grids of FY4A/AGRI satellite observations. Temporal interpolation is performed linearly between the two nearest ERA5 time steps, while spatial interpolation uses inverse distance weighting based on the four closest ERA5 grids to each satellite pixel. The matched atmospheric profiles, surface conditions, and geometric angles are then input into the ARMS model. The simulated reflectance under specific atmospheric and cloud conditions is utilized to generate look-up tables (LUTs), which support the retrieval of COT and CER for both liquid and ice phase clouds (Table 2). Fig. 2 illustrates the theoretical relationship between COT and CER for liquid clouds (a) and ice clouds (b) under fixed solar and viewing geometry. It can be seen that, for both cloud types, the reflectance in the visible and shortwave infrared channels generally increases with increasing COT and decreases with increasing CER. This behavior is consistent with previous studies (Letu et al., 2020; Zhuge et al., 2021).

Building upon these physical principles, this study proposes a novel retrieval algorithm for COT and CER, referred to as the DORF (Differential Operator-based Random Forest) algorithm, which integrates multispectral information with spatial structure features. Fig. 3 illustrates the structure and specific schematics of the DORF model. The core of the method is a Random Forest (RF) model that leverages both FY4A/AGRI multispectral observations and spatial gradient features to construct a nonlinear retrieval framework. The RF model has been widely used in environmental parameter estimation (Stafoggia et al., 2019). While its applications in cloud remote sensing are relatively limited compared to other networks, this study demonstrates that RF, when combined with physically meaningful spatial

features, can serve as an effective retrieval method for satellite- based cloud property estimation. In this framework, the RF model is trained with MODIS-retrieved COT and CER as the ground truth labels, whereas the prediction phase relies solely on FY4A/AGRI inputs. No MODIS data are used in prediction, thereby validating the transferability of the trained model to independent geostationary satellite observations.

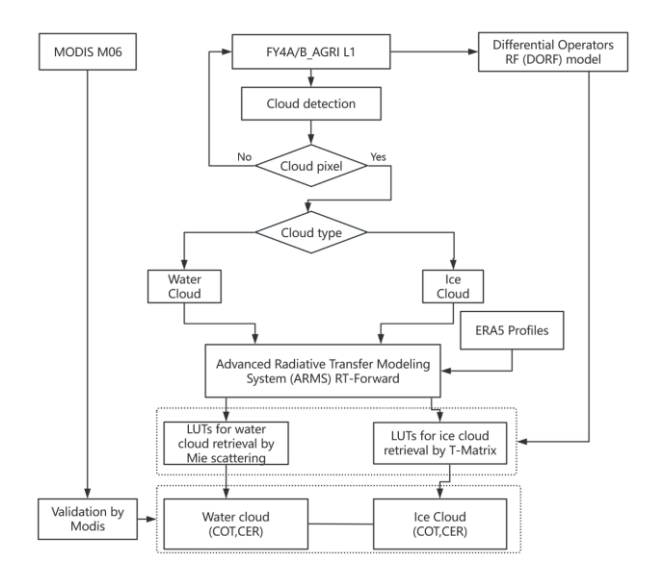
Specifically, six representative channels from the AGRI (i.e., channels 2, 5, 6, 7, 10, and 12) are selected to characterize the cloud's reflectance, absorption, and emission properties across different spectral bands. For each selected channel  $R^{i}$  (i=1, ...,6), we compute the first-order spatial gradients in the horizontal (x) and vertical (y) directions using the Sobel operator, yielding gradient magnitudes:

$$190 G_i = \sqrt{\left(\partial_x R_i\right)^2 + \left(\partial_y R_i\right)^2} (1)$$

The final input vector for each satellite pixel is then formulated as:

$$X = \left[ R_1, R_2, \dots, R_6, G_1, G_2, \dots, G_6 \right] \in R^{12}$$
 (2)

Where x denotes the combined spectral and spatial features, serves as input to the RF model. The Sobel operator is applied to each of the six selected AGRI channels using  $3\times3$  convolution kernels to approximate derivatives in the east-west and north-south directions. This magnitude reflects the local edge strength and spatial texture of the cloud field. Combined with the corresponding spectral reflectance values, they form the complete input vector x for the RF model. The nonlinear relationship between these features and the target cloud properties (COT and CER) is established using the MODIS official cloud products as the reference dataset.



200

185

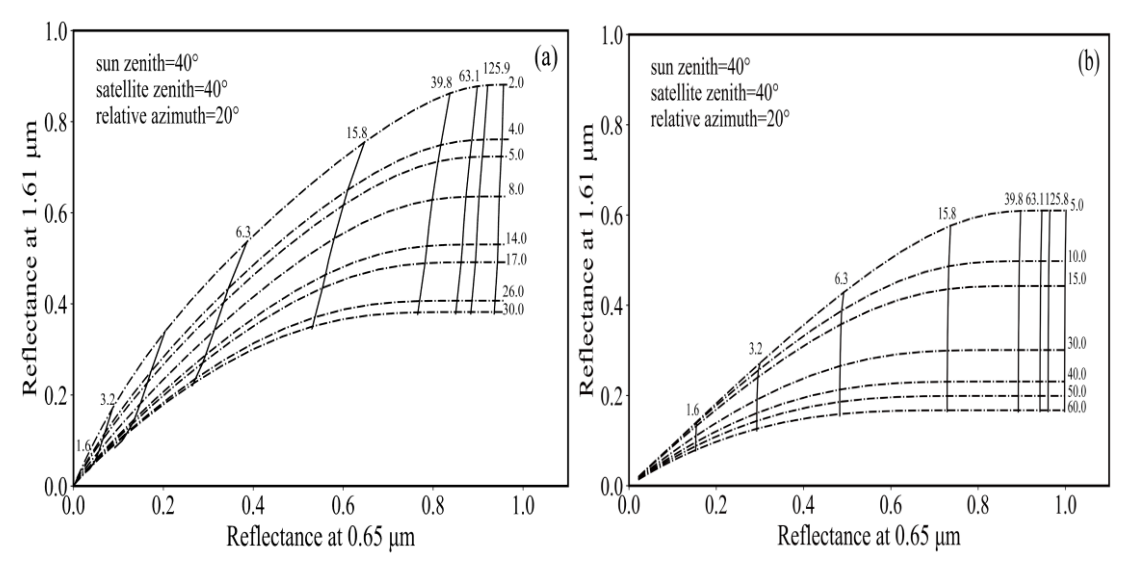
Figure 1. Framework of the COT and CER retrieval algorithm for FY4A AGRI

Table 1. Cloud detection thresholds for FY4A AGRI.

Channel	Physical significance	Threshold
$\frac{T_{0.65} - R_{0.825}}{R_{0.65} + R_{0.825}}$	Normalized Difference Cloud Index (NDCI)	>0.12
$R_{0.65}$	Reflectance	>0.3
$\frac{T_{0.65} - R_{1.61}}{R_{1.61} + R_{0.65}}$	Normalized Difference Snow Index (NDSI)	>0.26
$R_{0.47}$	Reflectance	>0.15

Table 2. Input parameters and grid points of the variables used to build the LUT version of the FY4A AGRI.

Variables	Range	Number	Unit
		of grids	
Sun zenith	0,5,10,15,20,25,30,35,40,45,50,55,60,65,70,75,80	15	degree
Satellite zenith	0,5,10,15,20,25,30,35,40,45,50,55,60,65,70,75,80	15	-
Relative Azimuth	0,10,20,30,40,50,60,70,80,90,100,110,120,130,140,150,1	19	-
	60,170,180		
Water cloud optical thickness	0.25, 0.32, 0.4, 0.5, 0.6, 0.8, 1.0, 1.26, 1.58, 1.99, 2.51, 3.16,	27	
	3.98,5.01,6.3,7.94,10.0,12.59,15.85,19.95,25.12,31.62,		
	39.81,50.12,63.1,79.4,100.0,125.9,158.5		
Water cloud effective radius	2,4,5,8,11,14,17,20,26,30,36,42,50,60	12	μm
Ice cloud optical thickness	0.25, 0.32, 0.4, 0.5, 0.6, 0.8, 1.0, 1.26, 1.58, 1.99, 2.51, 3.16,	27	
	3.98,5.01,6.3,7.94,10.0,12.59,15.85,19.95,25.12,31.62,		
	39.81,50.12,63.1,79.4,100.0,125.9,158.5		
Ice cloud effective radius	5,10,15,25,30,35,40,50,60,70,80,90,110,130	12	μm



**Figure 2.** Bispectral reflectance LUTs of cloud reflectance at 0.65 um and 1.61 um for water(a) and ice(b) phases when the solar zenith angle is 40°, the sensor viewing zenith angle is 40°, and the relative azimuth angle is 20°, and the underlying surface is land. The dashed line represents the CER, and the solid line represents the COT.

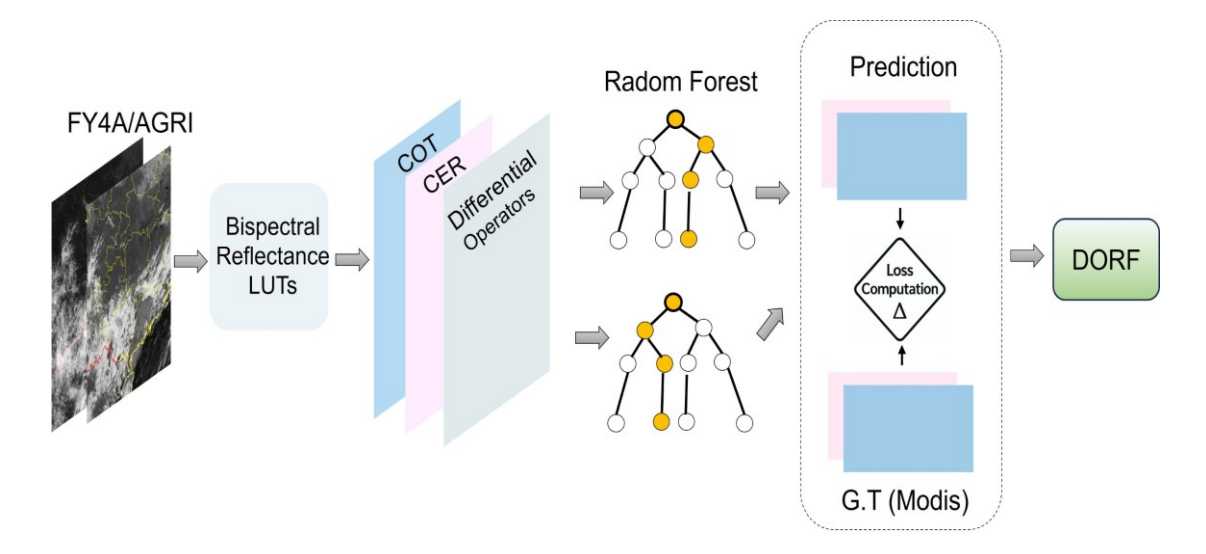


Figure 3. Schematic of the DORF model for COT and CER prediction based on FY-4A/AGRI observations.

## 3 COT and CER Retrievals and Comparisons

210

215

220

225

To evaluate the accuracy of FY4A/AGRI cloud property retrievals, we compared them with the MODIS Collection 6.1 MOD06 daytime cloud products from June to August 2018. For spatial matching, the 1 km MODIS pixels were averaged within each 4 km AGRI footprint to ensure consistent resolution. For temporal matching, the MODIS overpass was paired with the closest AGRI full-disk scan (15 min interval), with a maximum offset of ±7.5 min. The FY-4A/AGRI-derived CER exhibit strong consistency with the MODIS MOD06 results, with a coefficient of determination (R²) of 0.91, a mean absolute error (MAE) of 2.0 µm, and a root-mean-square error (RMSE) of 3.36 µm in Fig. 4. Similarly, the FY4A/AGRI-derived COT exhibits good consistency with MODIS MOD06, with R², MAE, and RMSE values of 0.87, 3.9, and 8.03, respectively.

Fig. 5 display the probability density distributions (PDFs)of CER and COT generated from the same 4 km resampled data to ensure consistency with Fig. 4. These PDFs provide a basis for comparing the retrievals between FY4A/AGRI and MODIS. The results indicate that FY4A/AGRI underestimates CER relative to MODIS for CER<13 μm, while it tends to retrieve larger CER values in the range of 14~23 μm. A similar trend is observed in COT, with MODIS yields higher values for COT<10 and FY4A/AGRI higher values at larger COT. These differences are mainly attributable to sensor resolution and the partial filling effect, whereby coarse pixels contain a mix of cloudy and clear areas (Chen and Fu, 2017; Ackerman et al., 2008; Chen et al., 2020). Overall, the distributions remain consistent, supporting the robustness of the retrievals.

To provide a concrete reference for subsequent perturbation experiments, we analyzed a mesoscale convective system (MCS) over central-eastern China on August 2, 2018. At 04:00 UTC, FY4A/AGRI false-color imagery revealed two isolated northward-moving convective cloud systems (Fig. 6a), with high-altitude ice clouds north of 30°N and low-level water clouds below (Fig. 6b). COT and CER retrievals from FY4A/AGRI and MODIS (Fig. 6c–f) show two high-value COT centers (>65) between 31–32.5°N and 111–113°E, with close agreement. For  $20 \le \text{COT} < 30$ , FY4A/AGRI slightly underestimates values (~12%). CER patterns are generally consistent, though differences appear in thin water cloud regions.

These differences mainly result from: (1) spatial resolution differences (MODIS 1 km vs. AGRI 4 km); (2) cloud horizontal inhomogeneity within AGRI pixels; and (3) visible channel degradation and SWIR fluctuations (Sun et al., 2025). Additionally, in the region 106–107°E, 32–35°N (corresponding to the Dabie and Wuling Mountains), FY4A/AGRI and MODIS retrievals show noticeable differences. This discrepancy is likely due to the influence of high-elevation terrain on satellite observations and the fact that the retrieval algorithm was primarily tuned for lowland surface types, without explicitly considering mountainous surface characteristics. Despite this local variation, the overall COT and CER patterns remain consistent within the common observed area. This case thus provides a robust reference for the perturbation experiments in Section 4.

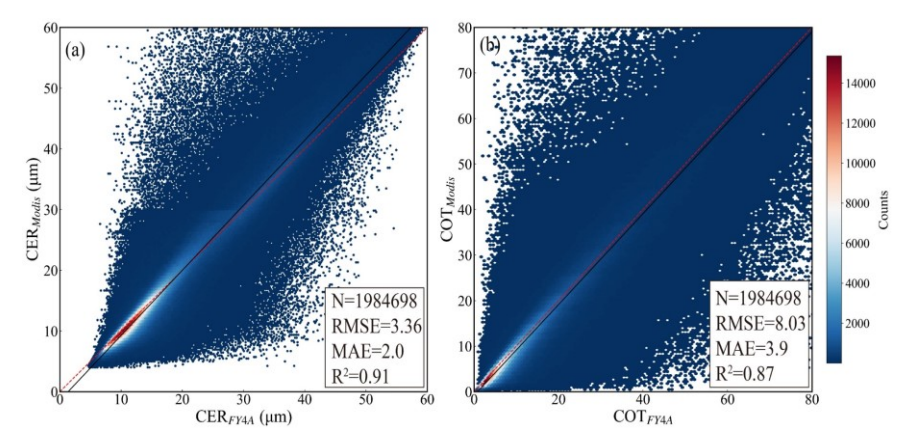


Figure 4. Scattering plot (a and b) of COT and CER from MODIS C6 (MOD06) and FY4A/AGRI data in the selected area.

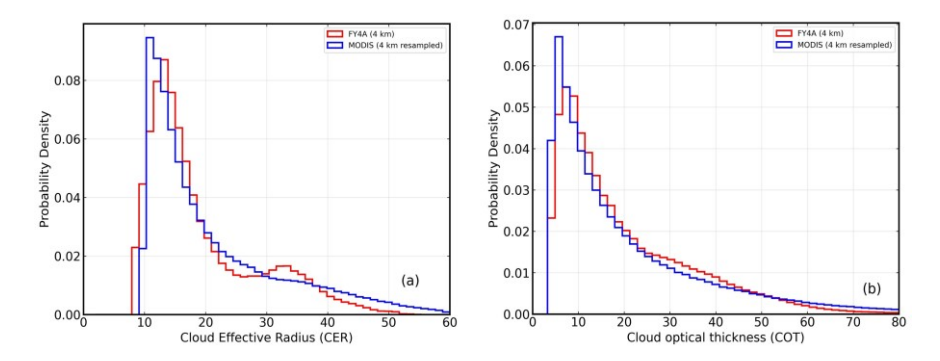
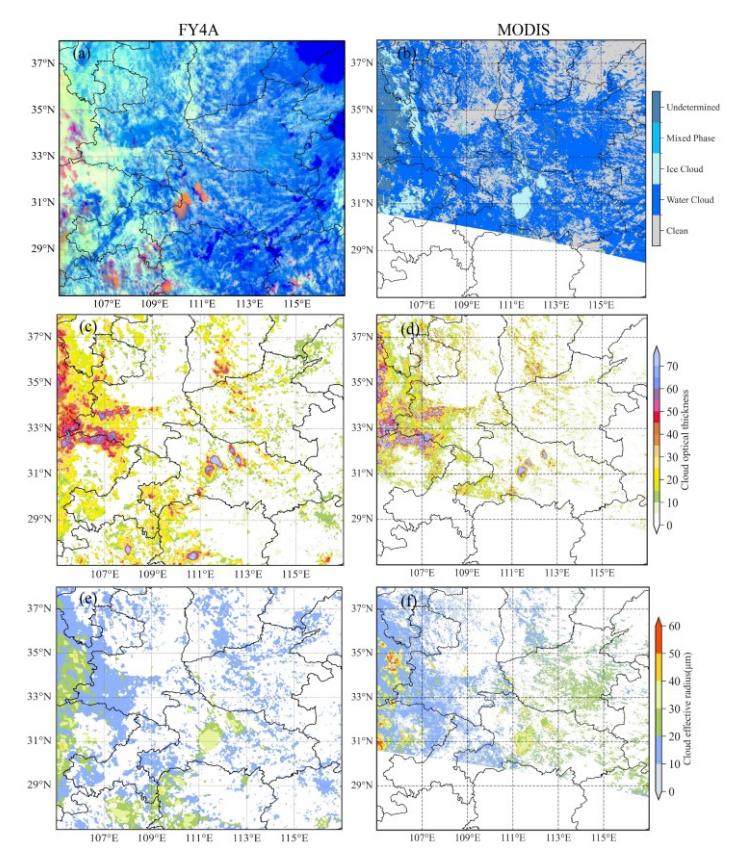


Figure 5. Probability density function (PDF) of the FY4A/AGRI retrieval results and the MODIS cloud products in the region. The red and black solid line shows the FY4A/AGRI results and the MODIS results, respectively.



**Figure 6.** Comparison of retrieved optical parameters using the FY-4 AGRI with MODIS cloud products (Cloud\_Optical\_Thickness\_16 and Cloud\_Effective\_Radius\_16). The observation time of the FY-4 AGRI is 04:00 UTC on 2 August 2018 and the MODIS observation time is 03:35 UTC. (a) False-color image (red, 0.65 μm; green, 1.61 μm; blue, 10.7 μm reversed) where thick ice clouds are orange colored, and low clouds are white colored. (b, d, f) cloud-top phase, COT(unitless), CER(unit: μm) from Collection-6.1 MOD06 at 0335 UTC August 2, 2018. (c,e) COT(unitless), CER(unit: μm) derived FY4A/AGRI at 0400 UTC August 2, 2018.

# 4 Cloud Microphysical and Radiation Response to Cloud Vertical Structure

255

260

Cloud vertical structure includes the number of cloud layers, cloud top height, cloud base height, cloud thickness, cloud fraction, and the vertical distribution of cloud microphysical properties. It reflects the thermodynamic, dynamic, and microphysical processes within the cloud system and plays an

important role in weather and climate (Xu et al., 2023). To quantitatively investigate the effects of cloud layer number and cloud phase on cloud reflectance, COT and CER, this study builds upon the case study retrieval results from Section 3.2. Cloud water profiles are categorized into single-layer, double-layer, and triple-layer clouds, and by adjusting the cloud liquid/ice water content in each layer, the sensitivity of cloud reflectance, COT and CER under different vertical cloud structure conditions is systematically analyzed.

## 4.1 Cloud water/ice content Profiles Classification

265

280

285

To investigate the impact of cloud vertical structure on COT and CER, 221 vertical profiles of cloud liquid and ice water content were extracted from ERA5 at 04:00 UTC on 2 August 2018 over the region 110~114°E and 30~33°N (Section 3.2). Based on empirical rules, each profile was classified into different structural types. The number of peaks in liquid/ice water content was used to determine the number of cloud layers, while cloud phase was inferred by pressure level: ice clouds above 450 hPa, and liquid clouds below 700 hPa and between 700–450 hPa.

Specifically, single-layer clouds, characterized by one peak, were divided into three types: high-level ice clouds, mid-level water clouds, and low-level water clouds. Two-layer cloud structures, identified by two peaks, were further categorized into five subtypes based on the cloud phase (ice or water) and the relative liquid or ice water content in the upper, middle, and lower layers. Three-layer profiles, indicated by three peaks, generally represent a typical ice—water—water cloud configuration (Fig. 7).

Statistical results (Table 3) show that single-layer clouds account for 48% of the profiles, two-layer clouds 46%, and three-layer clouds 6%. These proportions are consistent with the findings of Xu et al. (2023), who reported that single-layer clouds dominate (55.4%) in radiosonde observations, with two-layer systems being the most frequent among multilayer clouds. This agreement supports the validity and physical relevance of the classification method used.

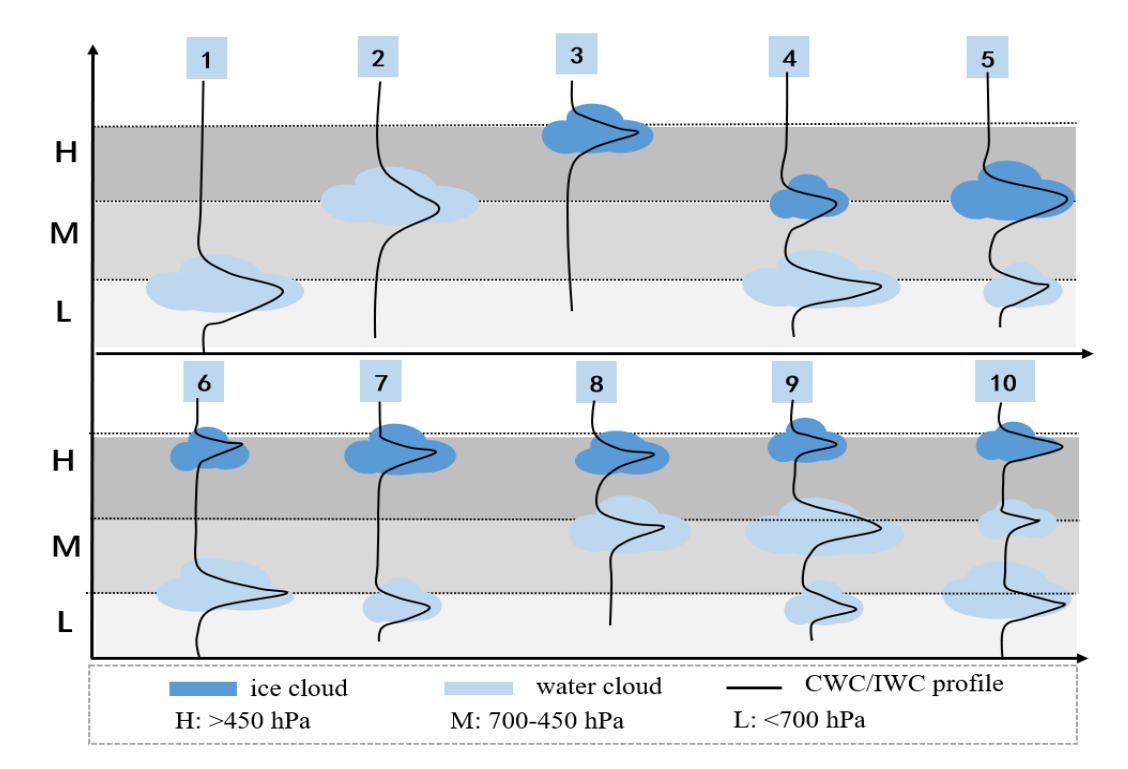


**Figure 7.** Vertical structure types of cloud water and ice content profiles from ERA5. The "large cloud" profiles correspond to the original profiles with a fivefold increase in cloud water or ice content, while the "small cloud" profiles represent the unmodified original profiles. The distinction between large and small clouds is not explicitly marked in the figure but can be inferred from the differences in water content.

**Table 3** Proportions of single-layer, two-layer, and three-layer Cloud Profiles and Corresponding Mode Classifications

Cloud	Height	Cloud	Exp	Ratio
Layers		type	No.	
Single	Н	Ice	3	
Layers	M	Water	2	48%
Cloud	L	Water	1	
	H+M	Ice +	8	
Two-layer		Water		46%
Clouds	H+L	Ice +	6,7	
		Water		
	L+M	Ice +	4,5	
		Water		
Three-	H+M+L	Ice +	9,10	6%
layer		Water		
Clouds		+Water		

## 4.2 Sensitivity of Reflectance to Cloud Vertical Structure

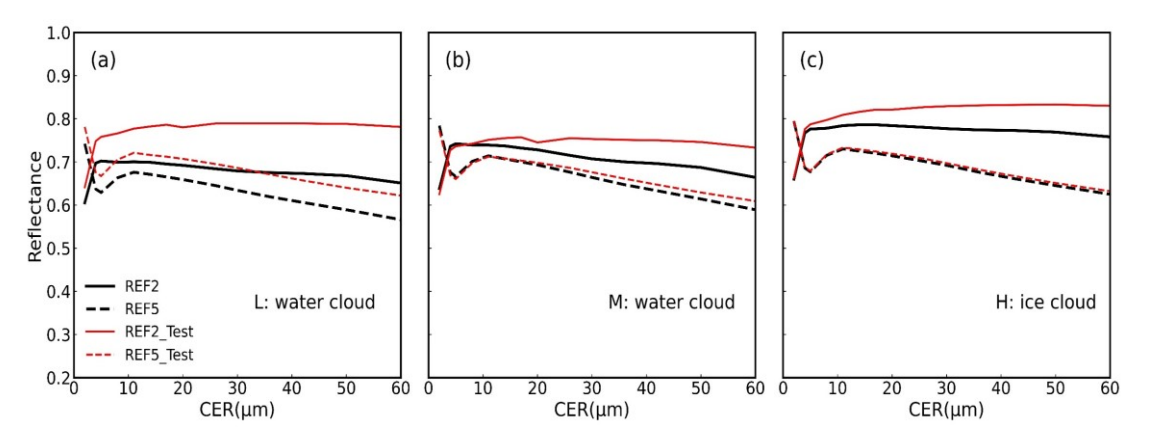
Based on the classification, the sensitivity experiments are designed to investigate how perturbations in cloud liquid water content (CWC) and ice water content (IWC) at different vertical levels (low, mid, and high) influence the reflectance responses of FY-4A/AGRI Channels 2 and 5. The vertical positions of the cloud layers are prescribed and fixed, so the variations in reflectance shown in Figs. 8–10 result from systematic changes in CWC and IWC at these levels, rather than from changes in cloud height alone. To ensure representativeness of each cloud type, the CWC and IWC vertical profiles used in the experiments were constructed from the mean profiles of ERA5 for each category.

Fig. 8 shows the sensitivity of cloud reflectance to CER variations for three single-layer cloud types under increased LWC or IWC. For low-level water clouds, channel 2 reflectance rises from 0.6 to 0.7 as CER increases from 2 to 10 μm, while channel 5 first decreases then rise to 0.68 (Fig. 8a). Increasing LWC enhances channel 2 reflectance by about 0.1, with a smaller effect on channel 5. Mid-level water clouds exhibit significant reflectance changes in channel 2 only when CER exceeds 10 μm, stabilizing beyond 25 μm (Fig. 8b). High-level ice clouds show slightly higher reflectance in both channels compared to water clouds (Fig. 8c). Overall, increased LWC in low-level clouds notably boosts reflectance, especially in the visible channel, by approximately 15% more than mid- or high-level clouds. Moreover, the minimal response of channel 5 reflectance for high-level ice clouds when increasing IWC is consistent with Wang et al. (2018), who showed that shortwave infrared (SWIR) channels are primarily weighted toward cloud top. If the top-layer CER is already large, additional IWC exerts little effect on SWIR reflectance.

For double-layer clouds, the reflectance response is determined by the combination of liquid and ice clouds. In the "mid-level water cloud–high-level ice cloud" configuration, channel 5 reflectance remains nearly unchanged under different perturbations, whereas channel 2 exhibits significant variations. For CER < 5 µm, increasing mid-level CWC or high-level IWC yields almost identical results; for CER > 5 µm, increasing high-level IWC produces slightly higher channel 2 reflectance than increasing mid-level CWC (Fig. 9a, d), likely due to multiple scattering in the upper ice cloud enhancing upward radiation while partially diminishing the mid-level water cloud contribution. In the "low-level water cloud–high-level ice cloud" configuration (Fig. 9c and f), the overall reflectance response is similar to that of the mid-level water cloud–high-level ice cloud case, indicating that the upper ice cloud dominates the system's radiative properties. This mechanistically supports the observational findings of Kiran et al. (2015), which reported that despite the presence of liquid water clouds at lower levels, the net radiative

forcing at the top of the atmosphere remains nearly balanced, primarily due to the simultaneous shortwave cooling and longwave heating effects of the upper ice cloud. By contrast, in the "low-level water cloud–mid-level ice cloud" configuration, the reflectance response to increases in CWC/IWC at different levels is markedly different from the previous two cases. Specifically, increasing low-level CWC causes channel 2 reflectance to vary nonlinearly with CER, first decreasing and then increasing (Fig. 9b), whereas increasing mid-level IWC results in a linear decrease of reflectance in both channels 2 and 5, with channel 5 even decreasing by approximately 0.12 when CER > 30 µm (Fig. 9e).

For the three-layer clouds consisting of high-level ice cloud over mid-level water cloud over low-level water cloud, increasing either low- or mid-level CWC enhances Channel 2 reflectance with increasing CER, with the increase being more pronounced for mid-level CWC (Fig. 10a-b). The response of Channel 5 reflectance exhibits a similar trend but with a smaller magnitude, indicating that the mid-level water cloud contributes more significantly to reflectance in both channels. When high-level IWC is increased, Channel 2 reflectance decreases approximately linearly with CER, while Channel 5 also declines (Fig. 10c). For CER >14 μm, Channel 5 reflectance drops from ~0.4 to 0.25, highlighting the strong radiative shielding effect of the high-level ice cloud on underlying water clouds. These observations align with Li et al. (2011), who found that multilayer clouds have weaker shortwave reflectance than single-layer clouds due to their higher cloud tops allowing shortwave radiation to partially transmit to lower clouds or the surface.



**Figure 8.** Variation of cloud reflectance at Channel 2 (solid lines) and Channel 5 (dashed lines) with cloud effective radius (CER) under different LWC or IWC condition. Black lines correspond to reflectance simulated using the original LWC/IWC profiles from ERA5 reanalysis, while red lines represent reflectance simulated with LWC/IWC increased by a factor of 5. Three single-layer cloud types are shown: low-level water clouds (a, Exp 1), mid-level water clouds (b, Exp 2), and high-level ice clouds (c, Exp 3). The simulations assume a solar zenith angle of 40°, sensor viewing zenith

angle of 40°, and relative azimuth angle of 20°.

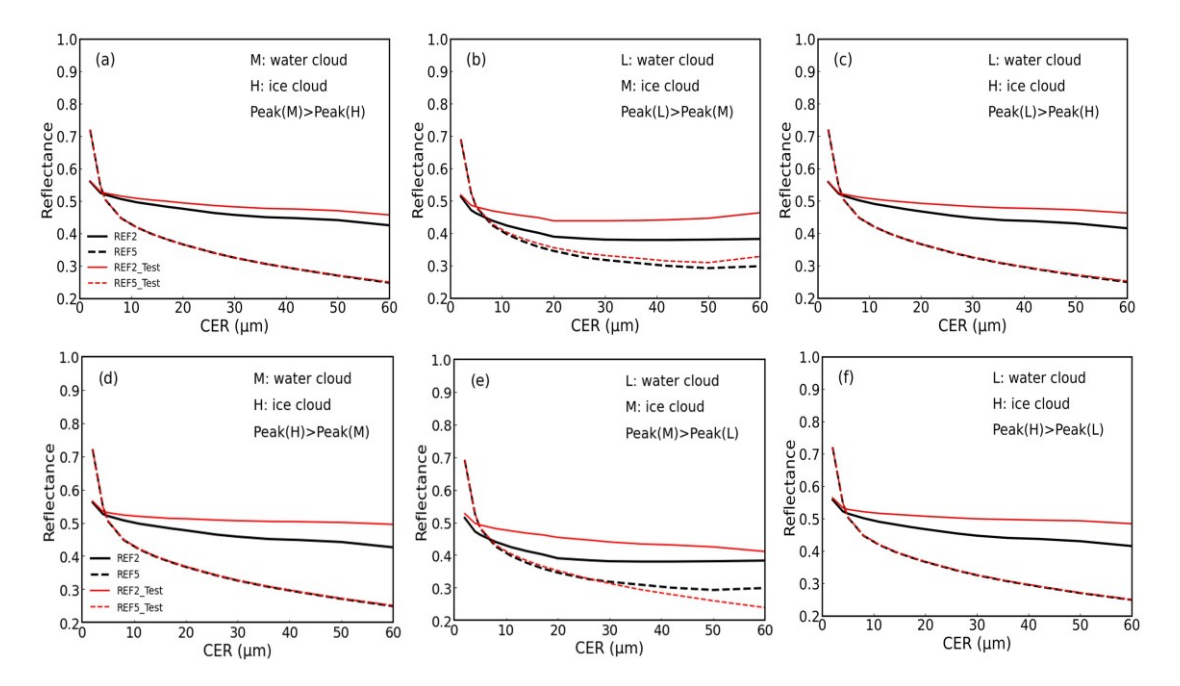


**Figure. 9.** Reflectance—CER relationships for six double-layer cloud sensitivity experiments: (a, d) mid-level water + high-level ice cloud, with (a) increased mid-level CWC (Exp 8) and (d) increased high-level IWC(Exp 8); (b, e) low-level water + mid-level ice cloud, with (b) increased low-level CWC(Exp 4) and © increased mid-level IWC(Exp 5); (c, f) low-level water + high-level ice cloud, with (c) increased low-level CWC(Exp 6) and (f) increased high-level IWC(Exp 7). Each panel illustrates the effect of adjusting cloud water content (CWC) or ice water content (IWC) on the reflectance—CER relationship for the corresponding cloud vertical structure.

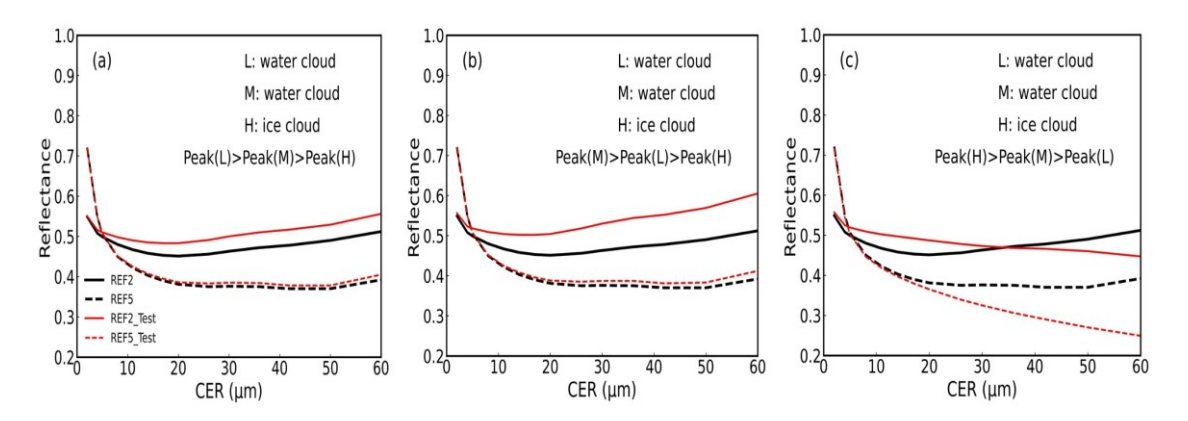


Figure 10. Similar to Fig. 9, but for multi-layer clouds (a) Exp 9 and (b) Exp 10.

## 4.3 Sensitivity of COT-CER Relationship to Cloud Vertical Structure

The operational COT and CER retrieval algorithm developed in Section 3 is based on single-layer cloud assumptions. In reality, cloud systems are frequently multi-layered, which can introduce significant uncertainties in retrievals. To quantify these effects, we conducted idealized perturbation experiments using representative single-, double-, and three-layer cloud configurations (Fig. 11), perturbing CWC or

360

IWC at specific vertical levels and comparing the resulting optical thickness ( $\Delta$ COT) with unperturbed cases.

370

375

380

385

390

395

For single-layer clouds,  $\Delta$ COT increases nonlinearly with CER, showing a rapid rise when CER is below 15 μm before approaching saturation. Notably, when CER < 10 μm, increasing LWC in mid-level water clouds leads to a maximum  $\Delta$ COT of 52, which is approximately 1.6 times greater than that resulting from the same perturbation in low-level clouds (Fig. 11b). For two-layer structures, three typical configurations were analyzed: (1) mid-level ice cloud over low-level water cloud (Fig. 11c), (2) highlevel ice cloud over low-level water cloud (Fig. 11d), and (3) high-level ice cloud over mid-level water cloud (Fig. 11e). On average, the COT increase due to low- and mid-level water cloud variations in single-layer clouds exceeds that in double-layer clouds by about 24%, primarily due to the masking effect of upper-level ice clouds in double-layer structures. Low-level water beneath mid-level ice showed negative ΔCOT at small CER, whereas high-level ice over low-level water enhanced ΔCOT. The highlevel ice over mid-level water scenario exhibited a non-monotonic ΔCOT pattern for small CER, likely due to complex radiative interactions between layers. For three-layer clouds, increases in mid- or lowerlevel CWC significantly enhance ΔCOT, although peak values are slightly lower than in single-layer clouds (Fig. 11e). The lower water layer dominates the response, while overlying ice partially masks the effect. These results agree with Wang et al. (2021), who showed that subgrid-scale cloud structure and overlapping condensate significantly modulate radiative effects.

We further examined the impact of multi-layer cloud vertical structures by comparing COT from idealized double- and triple-layer simulations with single-layer retrievals. Fig. 12 shows the difference between COT retrieved under the single-layer assumption and that simulated with multi-layer clouds ( $\Delta$ COT\_retrieval, hereafter abbreviated as  $\Delta$ COT\_R) as a function of CER. Overall, when CER < 10  $\mu$ m,  $\Delta$ COT\_R changes from negative to positive, indicating that the single-layer assumption systematically underestimates the true COT under small droplet conditions. As CER increases beyond 14  $\mu$ m,  $\Delta$ COT\_R gradually becomes positive, with single-layer retrievals exceeding two-layer simulations by approximately 20 units on average. This primarily results from the single-layer assumption's inability to capture the shielding effect of overlying ice clouds on underlying water clouds, as well as the differential contribution of particles at different vertical levels to reflectance in the visible and shortwave infrared channels.

For the "mid-level water cloud and high-level ice cloud" structure, ΔCOT R remains negative for

CER < 22  $\mu$ m before turning positive (Fig. 12a). For the "low-level water cloud and high-level ice cloud" structure, positive  $\Delta$ COT\_R appear only when CER > 45  $\mu$ m (Fig. 12b). Increasing the IWC of the high-level ice cloud maintains negative  $\Delta$ COT\_R at small CER, with the positive transition also at CER > 45  $\mu$ m. In the "low-level water and mid-level ice" scenario,  $\Delta$ COT\_R is near zero for CER < 5  $\mu$ m, increases gradually with CER, and plateaus beyond 30  $\mu$ m. The critical CER values where  $\Delta$ COT\_R changes sign depend on the perturbed layer: ~14  $\mu$ m for mid-level IWC and ~30  $\mu$ m for low-level CWC (Fig. 12c), consistent with reflectance sensitivity results.

For the three-layer cloud case, increasing mid-level CWC results in single-layer retrievals being consistently smaller than the simulations when CER < 50  $\mu$ m, highlighting the limitations of the single-layer assumption under complex vertical structures (Fig. 12d). Together with the preceding COT–CER analyses, these results quantitatively demonstrate that neglecting vertical heterogeneity introduces significant biases in single-layer retrievals, with both the magnitude and sign of  $\Delta$ COT\_R strongly dependent on CER and the vertical distribution, thickness, and microphysical properties of water and ice layers. Importantly, the trends observed in  $\Delta$ COT\_R are consistent with the reflectance sensitivity experiments, confirming the direct impact of vertical cloud structure on operational COT retrievals.

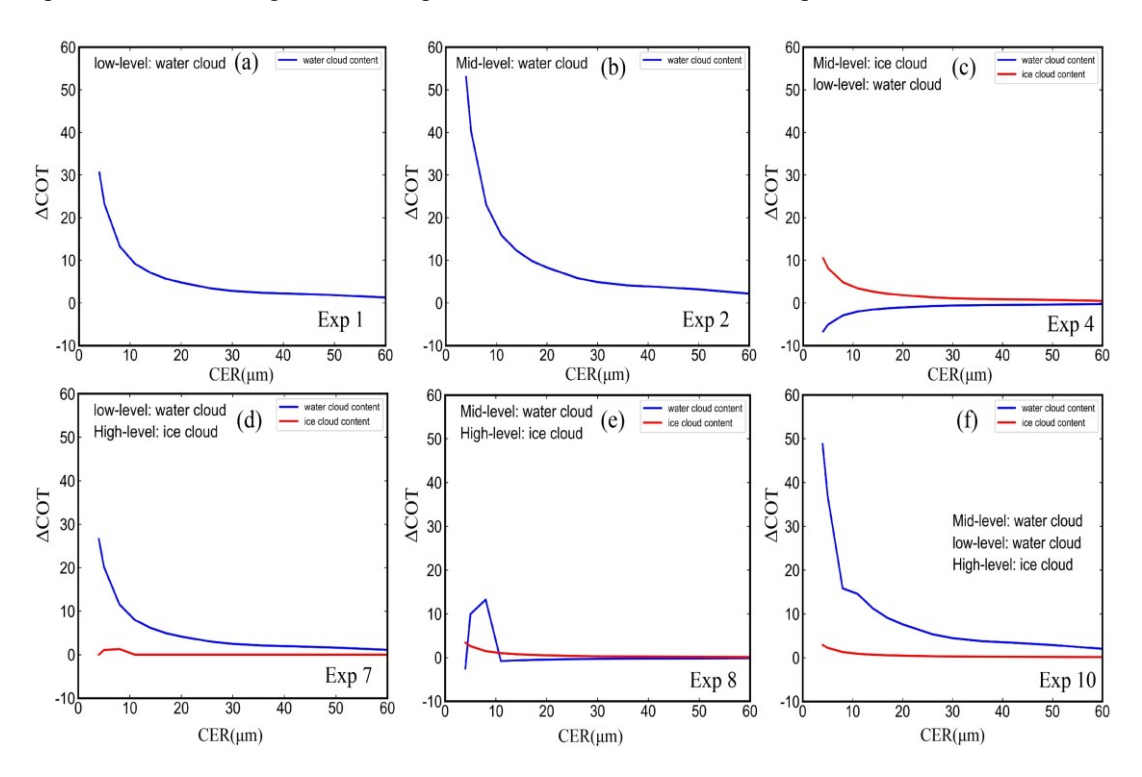


**Figure 11.** Changes in cloud optical thickness ( $\Delta$ COT) as a function of CER for six selected vertical cloud structure types (Exp 1, 2, 7, 8, and 10). Each panel shows the  $\Delta$ COT resulting from adding LWC or IWC to a specific vertical layer relative to a reference state without that layer. Blue lines represent the contribution of added LWC, while red lines represent added IWC. Model numbers are

indicated in each panel. when the solar zenith angle is  $40^{\circ}$ , the sensor viewing zenith angle is  $40^{\circ}$ , and the relative azimuth angle is  $20^{\circ}$ .

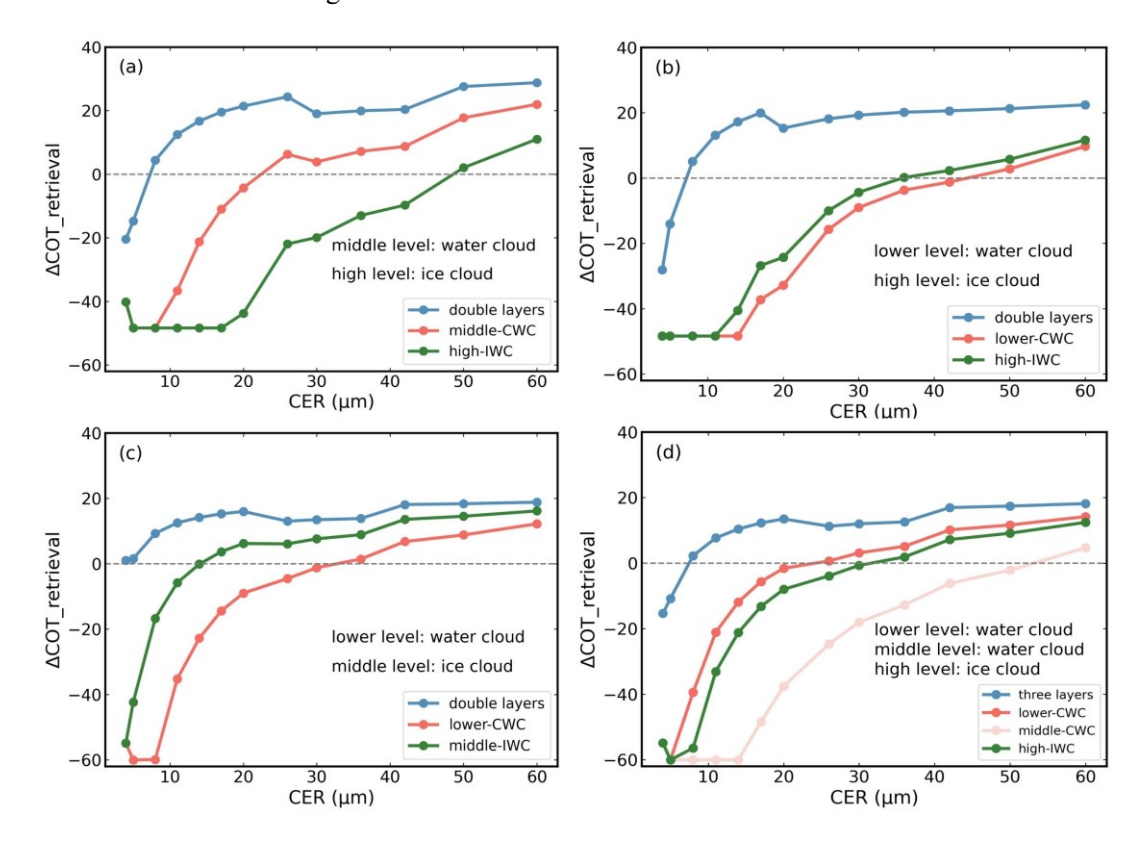


Figure 12. Differences in cloud optical thickness (COT) between multilayer cloud vertical structures and the single-layer assumption as a function of CER. Blue: difference between COT retrieved under the single-layer assumption and COT simulated for double-layer clouds; Red and pink: difference after adding CWC to the mid-level water cloud; Green: difference after adding IWC to the high-level ice cloud.

## 425 5 Summary and Conclusions

430

435

Based on FY4A/AGRI geostationary satellite observations over eastern and central China during June–August 2018, this study focuses on the influence of cloud vertical structure on the relationship between cloud optical thickness (COT) and cloud effective radius (CER). A bispectral retrieval algorithm for COT and CER was developed using the Advanced Radiative Transfer Modeling System (ARMS) and validated against MODIS cloud products. To systematically examine the impact of vertical cloud heterogeneity, ten idealized single-, double-, and three-layer cloud structures were constructed, allowing evaluation of how perturbations in cloud water content (CWC) and ice water content (IWC) at different altitudes affect both reflectance and the resulting COT–CER relationship.

The COT and CER retrieved from FY4A/AGRI show good agreement with MODIS, confirming its reliability for analyzing the sensitivity of COT and CER to cloud vertical structure. Figure 13 presents a conceptual schematic of the radiative effects of cloud layering. Cloud reflectance in the visible and

shortwave-infrared channels is influenced by CWC and IWC at different altitudes, as well as particle size. For single-layer liquid clouds, increasing low-level LWC strongly enhances reflectance, with visible channel increases about 15% greater than those for mid-level liquid or high-level ice clouds. In two-layer clouds, the "mid-level water—high-level ice" and "low-level water—high-level ice" configurations are dominated by the upper ice cloud, while in the "low-level water—mid-level ice" configuration, increasing low-level CWC first reduces and then increases reflectance, whereas increasing mid-level IWC causes a linear decrease. For three-layer clouds, mid- and low-level water clouds contribute most to the visible channel, while high-level IWC strongly reduces reflectance through radiative shielding.

Through idealized perturbation experiments on representative single-, double-, and triple-layer cloud structures, we quantified the impact of cloud vertical structure on the COT–CER relationship. Results show that for single-layer clouds,  $\Delta COT$  increases nonlinearly with CER, reaching a maximum at small particle sizes (CER < 15  $\mu m$ ). When CER < 10  $\mu m$ , an increase in mid-level water cloud LWC produces a  $\Delta COT$  of up to 52, approximately 1.6 times that of an equivalent perturbation in low-level clouds. For multi-layer clouds, overlying ice layers partially mask the radiative effects of lower water clouds, causing  $\Delta COT$  to be negative or non-monotonic at small CER. Further comparison between multi-layer simulations and single-layer retrievals shows that single-layer retrievals systematically underestimate COT at small CER, while at larger CER, the single-layer results exceed double-layer simulations by about 20 units on average. For the low-level water–mid-level ice cloud structure, the difference between retrieval and simulated results is close to 0 when CER < 5  $\mu m$ , gradually increases with CER, and plateaus for CER > 30  $\mu m$ , reflecting the sustained shielding effect of the upper ice layer on the lower water cloud. In triple-layer clouds, increasing mid-level CWC causes single-layer retrievals to remain below simulation values for CER < 50  $\mu m$ , further highlighting the limitations of the single-layer assumption under complex vertical structures.

These results suggest that assuming a single homogeneous cloud layer in remote sensing retrievals can cause significant errors. Upper-level ice clouds can shield lower-level water clouds, leading to underestimated total reflectance and systematic low bias in COT. CER retrievals are also sensitive to cloud layer height and water/ice content distribution, with neglect of inter-layer radiative effects increasing uncertainty. Sensitivity experiments indicate that for CER < 20 µm, the mean increase in COT caused by variations in single-layer clouds exceeds that in double-layer cloud structures by approximately 24%. Incorporating prior cloud vertical structure information from active sensors or

reanalysis can improve COT and CER retrieval accuracy, as well as provide guidance for obtaining more reliable retrievals under complex multilayer cloud conditions.

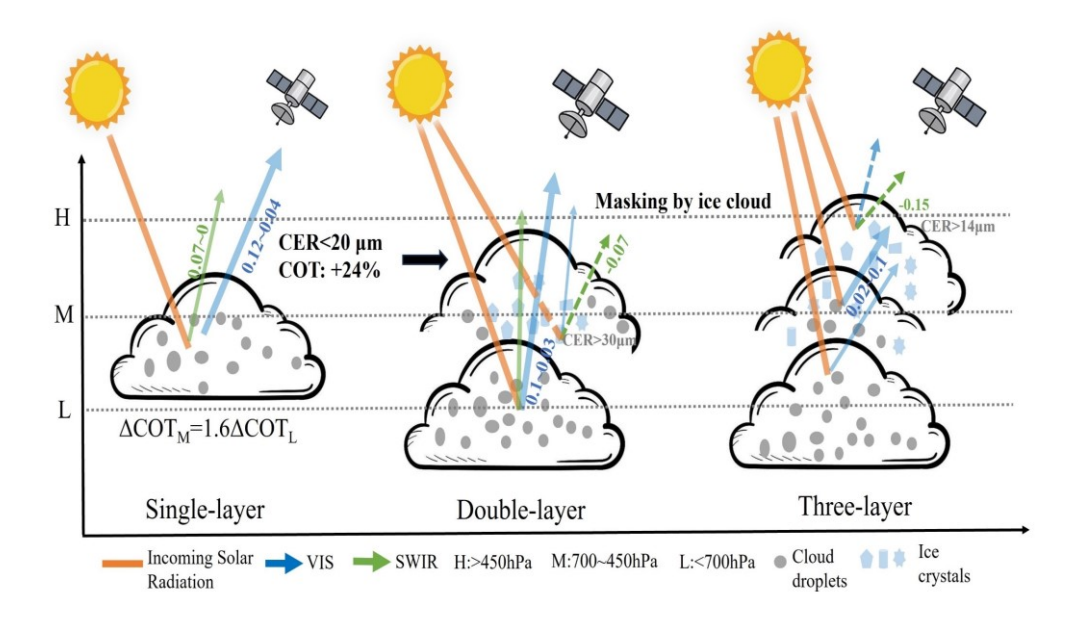


Figure 13. Conceptual diagram illustrating the radiative characteristics and retrieval implications of COT and CER under different vertical cloud structures.

Code availability. The code used in this study are available from the corresponding author upon reasonable request(ghlyy@mail.iap.ac.cn).

Data availability. The FY4A/AGRI data used for the main COT and CER retrieval in this study are 475 released from the Fengyun Meteorological Satellite Remote Sensing Data Service Platform (https://satellite.nsmc.org.cn/DataPortal/cn/data/order.html). The MODIS cloud product used for the DORF model building and for validating the spatial distributions of retrieved COT and CER from FY4A/AGRI(https://ladsweb.modaps.eosdis.nasa.gov/search/order/1/MOD06 L2--61,MYD06 L2--61). The ERA5 reanalysis data provided by the European Centre for Medium-Range Weather Forecasts 480 (ECMWF) are used to supply atmospheric temperature, humidity, and pressure profiles as input to the ARMS model (Hersbach et al., 2020). Additionally, vertical profiles of cloud liquid water and ice water content from ERA5 are used to construct and classify the idealized cloud vertical structure models used in the sensitivity experiments (https://cds.climate.copernicus.eu/datasets/). The Advanced Radiative Transfer Modeling System (ARMS) model developed in China (Weng et al., 2020), and the package is 485 available from hanyang@cma.gov.cn. The random forest technique is available at https://scikitlearn.org/stable/modules/generated/sklearn.ensemble.

**Author contributions.** JS conceptualized the study, and wrote the original draft. JS and YL designed the algorithms, and revised the manuscript. HH, QL, and CY validated results and supervised the research. YS and ZC performed the simulations.

Competing interests. The authors declare that they have no known competing financial interests or

personal relationships that could have appeared to influence the work reported in this paper.

Acknowledgements. The authors would like to thank the National Satellite Meteorological Center for providing the FY4A/AGRI Level-1 full-disk observation data, the National Aeronautics and Space Administration (NASA) Level-1 and Atmosphere Archive & Distribution System (LAADS) for providing the MODIS cloud products, the European Centre for Medium-Range Weather Forecasts (ECMWF) for the ERA5 reanalysis data. We also acknowledge the Numerical Weather Prediction Center of the China Meteorological Administration (CMA) for the development of the Advanced Radiative Transfer Modeling System (ARMS).

Financial support. This work was jointly supported by the Hunan Provincial Natural Science Foundation of China (grant number 2021JC0009), the National Natural Science Foundation of China (grant number U2242201), and the Hubei Provincial Natural Science Foundation of China (2025AFD423).

#### References

495

515

520

- Ackerman, S. A., Holz, R. E., Frey, R., Eloranta, E. W., Maddux, B. C., and Mcgill, M.: Cloud detection with MODIS. Part II: Validation, J. Atmos. Ocean. Tech., 25, 1073–1086, <a href="https://doi.org/10.1175/2007JTECHA1053.1">https://doi.org/10.1175/2007JTECHA1053.1</a>, 2008.
  - Bi, L. and Yang, P.: Improved ice particle optical property simulations in the ultraviolet to far-infrared regime. J. Quant. Spectrosc. Radiat. Transf. 189, 228–237, <a href="https://doi.org/10.1016/j.jqsrt.2016.12.007">https://doi.org/10.1016/j.jqsrt.2016.12.007</a>, 2017.
- Chen, Y., Weng, F., Han, Y., and Liu, Q.: Validation of the community radiative transfer model by using CloudSat data. J. Geophys. Res. Atmos. 113(D8), 114, <a href="https://doi.org/10.1029/2007JD009561">https://doi.org/10.1029/2007JD009561</a>, 2008.
  - Chen, Y., Chen, G., Cui, C., Zhang, A., Wan, R., Zhou, S., Wang, D., and Fu, Y.: Retrieval of the vertical evolution of the cloud effective radius from the Chinese FY-4(Feng Yun 4) next-generation geostationary satellites. Atmos. Chem. Phys. 20,1131-1145, <a href="https://doi.org/10.5194/acp-20-1131-2020">https://doi.org/10.5194/acp-20-1131-2020</a>, 2020.
  - Fang, L., Li, Y., Sun, G., Gao, C., and Lu, Z.: Horizontal and vertical distributions of clouds of different types based on CloudSat–CALIPSO data. Clim. Environ. Res. 21 (5): 547–556. <a href="https://doi:10.3878/j.issn.1006-9585.2016.15240">https://doi:10.3878/j.issn.1006-9585.2016.15240</a>, 2016.
  - Fu, Y.: Cloud parameters retrieved by the bispectral reflectance algorithm and associated applications, J. Meteorol. Res., 28, 965982, <a href="https://doi.org/10.1007/s13351-014-3292-3">https://doi.org/10.1007/s13351-014-3292-3</a>, 2014.
  - George, G., Sarangi, C., Tripathi, S. N., Chakraborty, T., and Turner, A.: Vertical Structure and Radiative Forcing of Monsoon Clouds Over Kanpur During the 2016 INCOMPASS Field Campaign, J. Geophys. Res.-Atmos. 123, 2152–2174, https://doi.org/10.1002/2017JD027759, 2018.
  - Hersbach, H., Bell, B., Berrisford, P., Hirahara, S., and Thépaut, J.: The ERA5 global reanalysis. Q. J. R. Meteorol. Soc. 146, 1999–2049, <a href="https://doi.org/10.1002/qj.3803">https://doi.org/10.1002/qj.3803</a>, 2020.
    - IPCC., Climate Change 2021. The Physical Science Basis. Contribution of Working Group I to the Sixth Assessment Report of the Intergovernmental Panel on Climate Change, Cambridge, United Kingdom and New York, NY, USA, Cambridge University Press. 2021.
- Lee, Y., Titov, D., Ignatiev, N., Tellmann, S., Patzold, M., Piccioni, G.: The radiative forcing variability caused by the changes of the upper cloud vertical structure in the Venus mesosphere, Planet. Space Sci. 113, 298–308, https://doi.org/10.1016/j.pss.2014.12.006, 2015.
  - Letu, H., Nagao, T., Nakajima, T., Riedi, J., Ishimoto, H., and Baran, A. J.: Ice cloud properties from

- Himawari-8/AHI next-generation geostationary satellite: Capability of the AHI to monitor the DC cloud generation process. IEEE Trans. Geos. Remote. Sen. 57(6), 1-11, https://doi.org/10.1109/TGRS.2018.2882803, 2018.
- Li, J., Yi, Y. H., Minnis, P., Huang, J., Yan, H., Ma, Y., Wang, W., and Ayers, J.: Radiative effect differences between multi-layered and single-layer clouds derived from CERES, CALIPSO, and CloudSat data. J. Quant. Spectrosc. Radiat. Transf. 112(2), 361-375, https://doi.org/10.1016/j.jqsrt.2010.10.006, 2011.
- Liu, C., Song, Y. X., Zhou, G. N., Teng, S. W., Li, B., Xu, N., Lu, F., and Zhang, P.: A cloud optical and microphysical property product for the advanced geosynchronous radiation imager onboard China's Fengyun-4 satellites: The first version. Atmos. Ocean. Sci. Lett. 16, 100337-100343, <a href="https://doi.org/10.1016/j.aosl.2023.100337">https://doi.org/10.1016/j.aosl.2023.100337</a>, 2023.

535

555

560

565

- Maddux, B., Ackerman, S., and Platnick, S.: Viewing Geometry Dependencies in MODIS Cloud Products, J. Atmos. Ocean. Tech. 27, 1519–1528, <a href="https://doi.org/10.1175/2010JTECHA1432.1">https://doi.org/10.1175/2010JTECHA1432.1</a>, 2010.
  - Matus, A., and L'Ecuyer, T.: The role of cloud phase in Earth's radiation budget. J. Geophys.Res.Atmos.122, 2559–2578, https://doi.org/10.1002/2016JD025951, 2017.
- Min, M, Wu, C., Li, C., Liu, H., Xu, N., Wu, X., Chen, L., Wang, F., Sun, F., Qin, D., Wang, X., Li, B.,
  Zheng, Z., Cao, G., and Dong, L.: Developing the Science Product Algorithm Testbed for Chinese Next-Generation Geostationary Meteorological Satellites: Fengyun-4 Series. J. Meteor. Res. 31, 708-719, https://doi.org/10.1007/s13351-017-6161-z, 2017.
  - Nakajima, T., and King, M.: Determination of the optical thickness and effective particle radius of clouds from reflected solar radiation measurements. Part I: Theory. J. Atmos. Sci. 47, 1878-1983, https://doi.org/10.1175/1520-0469(1990)047<1878:DOTOTA>2.0.CO;2, 1990.
  - Platnick, S., King, M., Ackerman, S., Menzel, W., Baum, B., Riédi, J., and Fery, R.: The MODIS cloud products: algorithms and examples from Terra. IEEE Trans. Geosci. Remote. Sens. 41 (2), 459–473, https://doi.org/10.1109/TGRS.2002.808301, 2003.
  - Platnick, S., Meyer, K. G., King, M.D., Wind, G., Amarasinghe, N., Marchant, B., Yang, P., Ridgway, W., Riedi, J.: The MODIS cloud optical and microphysical products: Collection 6 updates and examples from Terra and Aqua. IEEE Trans. Geosci. Remote. Sens. 55 (1), 502–525. https://doi.org/10.1109/TGRS.2016.2610522, 2017.
    - Ravi Kiran, V., Rajeevan, M., Gadhavi, Vijaya Bhaskara Rao, S., H., Jayaraman, A.: Role of vertical structure of cloud microphysical properties on cloud radiative forcing over the Asian monsoon region. Clim Dyn 45, 3331–3345, https://doi.org/10.1007/s00382-015-2542-0, 2015.
    - Saunders, R., Hocking, J., Turner, E., Rayer, P., Rundle, D., Brunel, P., Vidot, J., Roquet, P., Matricardi, M., Geer, A., Bormann, N., and Lupu, C.: An update on the RTTOV fast radiative transfer model. Geosci. Model. Dev., 11(7): 2717-2737, <a href="https://doi.org/10.5194/gmd-11-2717-2018">https://doi.org/10.5194/gmd-11-2717-2018</a>, 2018.
- Sourdeval, O., Laurent, C-L., Baran, A. J., and Gérard, B.: A methodology for simultaneous retrieval of ice and liquid water cloud properties. Part 2: Near-global retrievals and evaluation against A-Train products. Q. J. R. Meteorol. Soc. 142(701): 3063-3081, <a href="https://doi.org/10.1002/qj.2405">https://doi.org/10.1002/qj.2405</a>, 2016.
  - Stafoggia, M., Bellander, T., Bucci, S., Davoli, M., de Hoogh, K., de' Donato, F., Gariazzo, C., Lyapustin, A., Michelozzi, P., and Renzi, M.: Estimation of daily PM10 and PM2.5 concentrations in Italy, 2013–2015, using a spatiotemporal land-use random-forest model. Environ. Int. 124, 170–179, <a href="https://doi.org/10.1016/j.envint.2019.01.016">https://doi.org/10.1016/j.envint.2019.01.016</a>, 2019.

- Sun, C., Liu, C., Lu, F., Wang, F.K., Xu, R., Wang Z.W., Tang, S.H., Sohn, B.: Examination of Long-Term Fengyun-4 AGRI Reflective Solar Bands Calibration Using Cloud Targets. IEEE Transactions on Geoscience and Remote Sensing, 63. DOI:10.1109/TGRS.2025.3585943, 2025.
- Suzuki, K., Nakajima, T. Y., Stephens, G. L.: Particle growth and drop collection efficiency of warm clouds as inferred from joint CloudSat and MODIS observations. J. Atmos. Sci. 67 (9), 3019 3032, https://doi.org/10.1175/2010JAS3463.1, 2010.

585

- Tang, F., Zhuge, X., Zeng, M., Li, X., Dong, P., and Han, Y.: Applications of the Advanced Radiative Transfer Modeling System (ARMS) to Characterize the Performance of Fengyun–4A/AGRI. Remote. Sens.13, 3120-3143, https://doi.org/10.3390/rs13163120, 2021.
- Teng, S., Liu, C., Zhang, Z., Wang, Y., Sohn, B. J., and Yung, Y. L.: Retrieval of ice over water cloud microphysical and optical properties using passive radiometers. Geophys. Res. Lett. 47, e2020GL088941, <a href="https://doi.org/10.1029/2020GL088941">https://doi.org/10.1029/2020GL088941</a>, 2020.
- Teng, S., Liu, C., Tan, Z., Li, J., Xu, N., Hu, X., Zhang, P., Yan, W., Sohn, B.: A multispectral method for retrieving overlapping cloud top heights from passive radiometers. Remote. Sens. Envi. 286, 113425, https://doi.org/10.1016/j.rse.2022.113425, 2023.
  - Walker, J., MacKenzie, W., Mecikalski, J., and Jewett, C.: An Enhanced Geostationary Satellite–Based Convective Initiation Algorithm for 0–2-h Nowcasting with Object Tracking. J. Appl. Meteorol. Climatol. 51(11), 1931-1949, <a href="https://doi.org/https://doi.org/10.1175/JAMC-D-11-0246.1">https://doi.org/https://doi.org/https://doi.org/https://doi.org/10.1175/JAMC-D-11-0246.1</a>, 2012.
- Wang, C., Platnick, S., Fauchez, T., Meyer, K., Zhang, Z.B., Iwabuchi, H., Kahn, B.H.: An Assessment of the Impacts of Cloud Vertical Heterogeneity on Global Ice Cloud Data Records from Passive Satellite Retrievals. Journal of Geophysical Research: Atmospheres, 124(3):1578-1595. https://doi.org/10.1029/2018JD029681, 2019.
- Wang, J., Liu, C., Min, M., Hu, X., Lu, Q., and Letu, H.: Effects and applications of satellite radiometer 2.25-µm channel on cloud property retrievals. IEEE Trans. Geos. Remote. Sen. 56 (9), 5207–5216, https://doi:10.1109/tgrs.2018.2812082, 2018.
  - Weng, F., Yu, X., Duan, Y., Yang, J., Wang, J.: Advanced radiative transfer modeling system (ARMS): A new-generation satellite observation operator developed for numerical weather prediction and remote sensing applications. Adv. Atmos. Sci. 37, 131–136, <a href="https://doi.org/10.1007/s00376-019-9170-2">https://doi.org/10.1007/s00376-019-9170-2</a>, 2020.
  - Wang X., Miao H., Liu, Y., Bao, Q.: Dependence of cloud radiation on cloud overlap, horizontal inhomogeneity, and vertical alignment in stratiform and convective regions. Atmos. Res., 249:105358-105269, 2021.
- Xu, H., Guo, J., Tong, B., Zhang, J., Chen, T., Guo, X., Zhang, J., and Chen, W.: Characterizing the near-global cloud vertical structures over land using high-resolution radiosonde measurements. Atmos. Chem. Phys. 23, 15011–15038, https://doi.org/10.5194/acp-23-15011-2023, 2023.
  - Yuan, T., and Oreopoulos, L.:On the global character of overlap between low and high clouds. Geophys. Res. Lett. 40(19): 5320-5326, <a href="https://doi.org/10.1002/grl.50871">https://doi.org/10.1002/grl.50871</a>, 2013.
- Yang, J., Ding, S., Dong, P., Bi, L., Yi, B.: Advanced radiative transfer modeling system developed for satellite data assimilation and remote sensing applications, J. Quant. Spectrosc. Radiat. Transf. 251,107043, <a href="https://doi.org/10.1016/j.jqsrt.2020.107043">https://doi.org/10.1016/j.jqsrt.2020.107043</a>, 2020.
  - Yang, J., Zhang, Z. Q., Wei, C. Y., Lu, F., and Guo, Q.: Introducing the new generation of Chinese geostationary weather satellites, FENGYUN-4, Bull. Am. Meteorol. Soc. 98, 1637–1658, <a href="https://doi.org/10.1175/BAMS-D-16-0065.1">https://doi.org/10.1175/BAMS-D-16-0065.1</a>, 2017.

Zhao, C., Chen, Y., Li, J., Letu, H., Su, Y., Chen, T., and Wu, X.: Fifteen-year statistical analysis of cloud characteristics over China using Terra and Aqua Moderate Resolution Imaging Spectroradiometer observations. Int. J. Climatol. 39, 2612-2629, <a href="https://doi.org/10.1002/joc.5975">https://doi.org/10.1002/joc.5975</a>, 2018.

- Zhuge X., Zou, X., and Wang, Y.: A Fast Cloud Detection Algorithm Applicable to Monitoring and Nowcasting of Daytime Cloud Systems. IEEE Trans. Geosci. Remote. Sen. 55, 6111-6119, <a href="https://10.1109/TGRS.2017.2720664">https://10.1109/TGRS.2017.2720664</a>, 2017.
- Zhuge, X., and Zou, X.: Summertime Convective Initiation Nowcasting over Southeastern China Based on Advanced Himawari Imager Observations. J. Meteor. Soc. Japan. Ser. II, 96(4), 337-353, <a href="https://doi.org/10.2151/jmsj.2018-041">https://doi.org/10.2151/jmsj.2018-041</a>, 2018.
- Zhuge, X., Zou, X., and Wang, Y.: AHI-derived daytime cloud optical/microphysical properties and their evaluations with the colletion-6.1 MOD06 Product. IEEE Trans. Geos. Remote. Sen. 59, 6431-6450, https://doi.org/10.1109/TGRS.2020.3027017, 2021.